Science Advances
AAAS

advances.sciencemag.org/cgi/content/full/6/44/eabd0460/DC1

Supplementary Materials for

Hyperspectral infrared microscopy with visible light

Anna V. Paterova, Sivakumar M. Maniam, Hongzhi Yang, Gianluca Grenci*, Leonid A. Krivitsky*

*Corresponding author. Email: leonid_krivitskiy@imre.a-star.edu.sg (L.A.K.); mbigg@nus.edu.sg (G.G.)

Published 30 October 2020, *Sci. Adv.* **6**, eabd0460 (2020)
DOI: 10.1126/sciadv.abd0460

This PDF file includes:

Supplementary Materials

1. *The optical configuration of the wide-field microscope*

The working principle of the imaging system is shown in Fig. S1. Each mode of the SPDC with a given *k*-vector is generated with a Gaussian intensity distribution (*50*). Thus, the spatial resolution of the system is defined as follows:

$$\Delta\rho_k = \frac{\lambda_i}{2NA} = f_1 \frac{\lambda_i}{2nr}, \qquad \text{(S1)}$$

where λ_i is the wavelength of the idler photons, *NA* is the numerical aperture, f_1 is the focal length of the lens, *r* is the radius of the beam, *n* is the refractive index of the medium where the beam propagates.

The corresponding field of view (*FOV*) of the imaging system is given by:

$$FOV = 2 f_1 \theta_{\max}, \qquad \text{(S2)}$$

where $\theta_{\max}$ is the maximum emission angle of the SPDC (within a given spectral range), typically a few degrees, where one can still observe interference pattern.

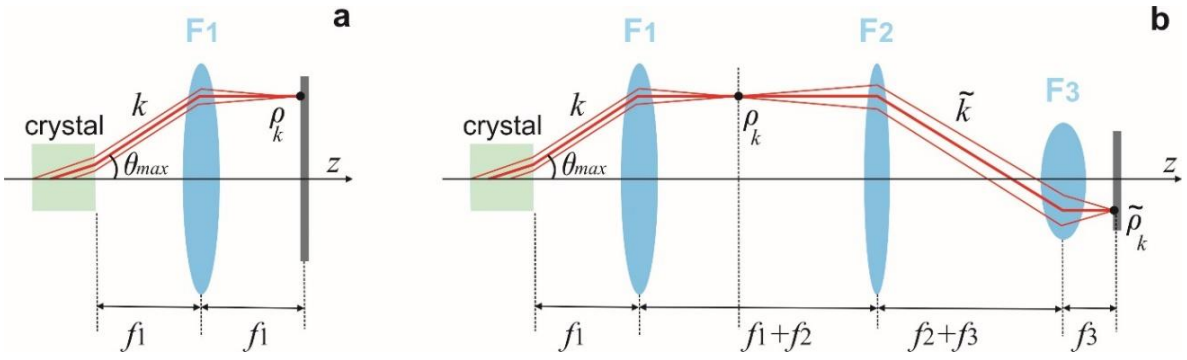

Fig. S1. Light propagation in the interferometer arm. The imaging system in one of the arms of the interferometer consisting of (**A**) one and (**B**) three lenses. In **A**, the crystal and the sample are placed at a focal distance from the lens F_1. In **B**, lenses F_1, F_2 and F_3 with

their respective focal length of f_1, f_2, and f_3 are positioned confocally. The parameters of the three-lens system define the spatial resolution of the method. The beams reflected from the sample (and reference mirror) take reciprocal paths as the original beams emitted from the crystal.

Equation (S1) suggests that a higher resolution can be achieved by decreasing f_1. However, choosing the lens with small f_1 is not practical, because it does not allow placing a dichroic beam splitter after the crystal. Hence, we insert two additional confocal lenses to achieve the desired resolution, see Fig. S1B. The first lens F_1 is placed at a focal distance f_1 from the crystal; the second lens F_2 with the focal distance f_2 is placed at a distance f_1+f_2 from the first lens, and the third lens F_3 with the focal distance f_3 is placed at a distance f_2+f_3 from the second lens. The sample is placed at the focal distance of the third lens f_3. The three-lens system in each arm of the interferometer projects the *k*-spectrum of signal and idler photons on the mirror and the sample, respectively.

The resolution and the field of view after the three-lens system are given by:

$$\begin{cases} \Delta\rho_k' = \dfrac{f_1 f_3}{f_2}\dfrac{\lambda_i}{2nr} \\ FOV' = 2\dfrac{f_1 f_3}{f_2}\theta_{\max} \end{cases}. \qquad \text{(S3)}$$

According to Eq. (S3), smaller f_1 and f_3, and larger f_2 are required to achieve the higher resolution.

2. <u>The intensity of signal photons in the nonlinear interferometer</u>

In the nonlinear interferometers, the SPDC process takes place in two nonlinear crystals (or within multiple passes of the pump through the nonlinear crystal). In the case of two identical nonlinear crystals, the state vector of SPDC light is given by (*19, 28, 34*):

$$|\psi\rangle = |vac\rangle + \xi \sum_{\omega_s,\omega_i} F(\omega_s,\omega_i) a_{s1}^{+} a_{i1}^{+} |vac\rangle + \xi e^{i\varphi_p} \sum_{\omega_s,\omega_i} F(\omega_s,\omega_i) a_{s2}^{+} a_{i2}^{+} |vac\rangle , \quad \text{(S4)}$$

where ξ is the efficiency of SPDC generation, $F(\omega_s,\omega_i)$ is the two-photon amplitude, $\omega_{s,i}$ are frequencies of the generated signal and idler SPDC photons, $a_{s,i}^{+}$ are photon generation operators for the signal (s) and idler (i) photons, respectively, s1,2 and i1,2 are the spatial modes of down-converted photons, φ_p is the relative phase acquired by the pump photon in the interferometer.

When the modes of the idler photons from the first i1 and the second i2 crystals are aligned, one can express the operator a_{i2} in terms of a_{i1}. Using the beam splitter model for describing losses for idler photons propagating from first to the second crystal, we can write the following expression:

$$a_{i2} = e^{i\varphi_i'} \left(t_i a_{i1} + r_i a_0 \right), \quad \text{(S5)}$$

where t_i is the complex transmission coefficient of idler photons on the way from first crystal to the second one, a_0 is the vacuum field entering from the empty port of the beam splitter with the complex reflection coefficient r_i, φ_i' is the phase acquired by the photon in mode i1. Taking into account Eq. (S5), the resulting state vector in Eq. (S4) is given by:

$$|\psi\rangle = |vac\rangle + \xi \sum_{\omega_s,\omega_i} F(\omega_s,\omega_i) a_{s1}^{+} a_{i1}^{+} |vac\rangle + \xi e^{i\varphi_p - i\varphi'} \sum_{\omega_s,\omega_i} F(\omega_s,\omega_i) a_{s2}^{+} \left(t_i^{*} a_{i1}^{+} + r_i^{*} a_0^{+} \right) |vac\rangle , \quad \text{(S6)}$$

The intensity of signal photons is given by:

$$I_s \propto \langle \psi | E_s^{(-)} E_s^{(+)} | \psi \rangle , \quad \text{(S7)}$$

where $E_s^{(+)}(t) \propto \sum_{\omega} a_{s1}(\omega) e^{-i\omega(t-t_1)} + a_{s2}(\omega) e^{-i\omega(t-t_2)}$ is the field reaching the detector, $t_{1,2}$ are the travel times of signal photons from the first and second crystals to the detector, respectively. Then, we can determine the following expression:

$$E_s^{(+)}|\psi\rangle \propto \sum_{\omega_s,\omega_i} F(\omega_s,\omega_i)\left[a_{i1}^{+}e^{-i\omega_s(t-t_1)}+ \right.$$
$$\left. +e^{-i\omega_s(t-t_2)+i(\varphi_p-\omega_i t_0)}\left(t_i^{*2}a_{i1}^{+}+r_i^{*}a_0^{+}\right)\right]|vac\rangle . \quad \text{(S8)}$$

Using Eqs. (S7) and (S8), the intensity of signal photons is given by (*34*):

$$I_s \propto 2\left[1+|t_i||\mu(\Delta t)|\cos\left(\varphi_p-\varphi_s-\varphi_i+\arg t^2+\arg\mu(\Delta t)\right)\right], \quad \text{(S9a)}$$

$$\mu(\Delta t)=\int|F(\Omega)|^2 e^{-i\Omega\Delta t}d\Omega, \quad \text{(S9b)}$$

where $\varphi_{s,i}$ is the phases accrued by signal and idler photons in the interferometer, respectively, $\mu(\Delta t)$ is the normalized first-order correlation function of the SPDC light, $\Delta t=t_0-t_2-t_1$ is the time delay (t_0 is the travel time of idler photons from crystal to the second one), Ω is the detuning frequency of SPDC photons from the central frequencies (*19, 28, 34*). Equation (S9a) is obtained considering a single spatial mode of SPDC light. Taking into account multiple spatial modes, the interference pattern can be expanded depending on the transverse coordinates ρ_{k_i}, see Eq. (1) in the main text for details.

3. *Experimental study of the spatial resolution*

Figures S2A,B show the interference patterns acquired at the relative phase $\varphi_i=0$ and $\varphi_i=\pi$, respectively. The contrast of the interference patterns is proportional to the amplitude reflectivity of the sample. Uncoated regions of the sample (glass substrate) show lower contrast than the background (chromium coated). The difference can be seen in Fig. S2C,D, which shows interference fringes from the chromium coated (red pixel in Fig. S2A,B) and glass surfaces (gray pixel in Fig. S2A,B), respectively.

Next, we plot the visibility maps across the sample, see Fig. S3A. Then, by comparing the obtained visibility map with the reference, acquired using a gold mirror as a sample (see Fig. S3B), we infer the reflectivity of the sample, see Fig. S3C.

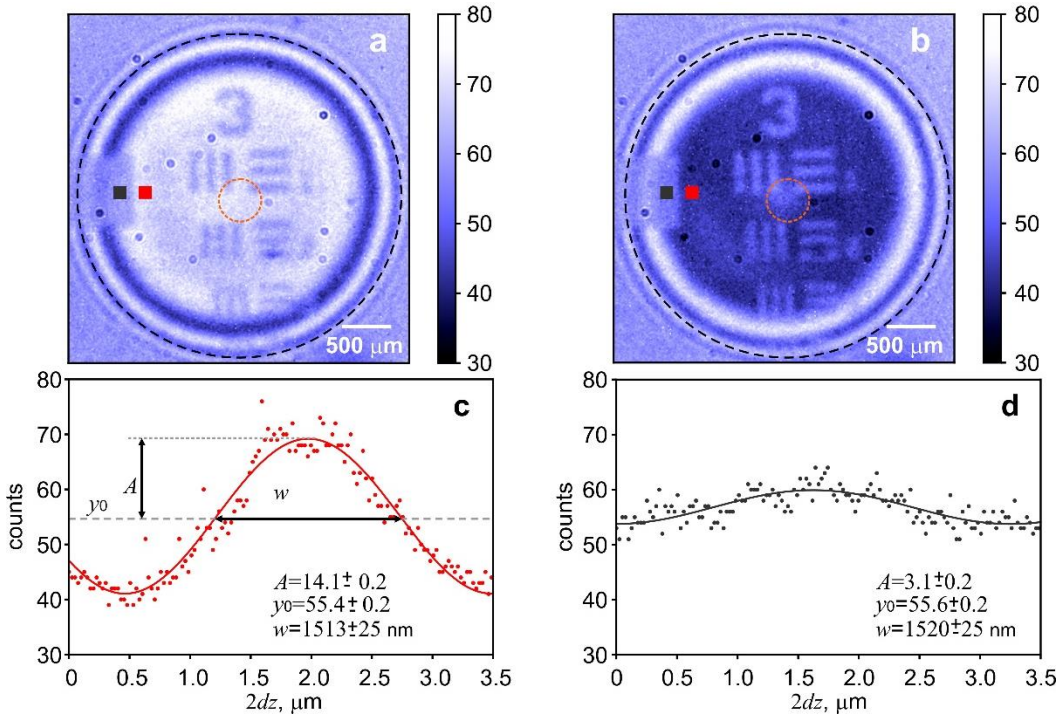

Fig. S2. Interference patterns obtained with a resolution test target. Single interference patterns produced by the resolution test target at the relative phase (**A**) $\varphi_i=0$ and (**A**) $\varphi_i=\pi$. The patterns are obtained using the lens F_3 with focal length of f_3=15 mm. (**C**) and (**D**) show interference fringes measured as a function of the path length difference for the reflective chromium region (red pixel in **A**,**B**) and the glass substrate (gray pixel in **A**,**B**), respectively. The wavelength of the probe photon is 3 μm and the detected photon is 647 nm.

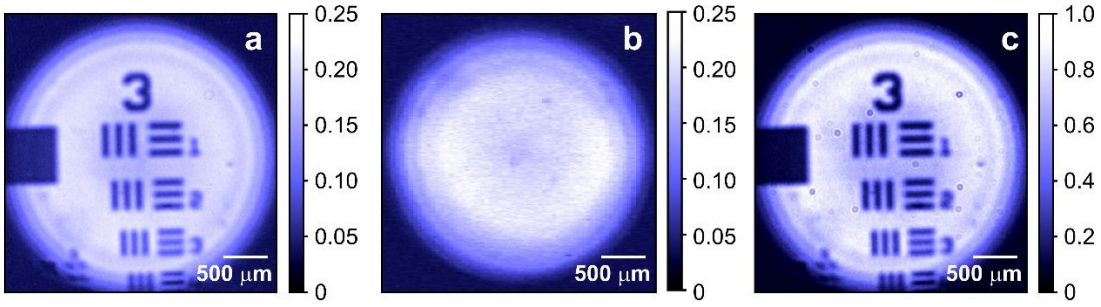

Fig. S3. Reflectance measurements of test samples. (**A**) The visibility map of the interference pattern obtained using the resolution test target obtained from 140 interference patterns, see Fig. S2. (**B**) The reference visibility map acquired with the gold mirror. (**C**)

The inferred reflectivity of the resolution test target. The wavelength of the probe photon is 3 μm and the detected photon is 647 nm.

4. The spectrum of SPDC photons

The measured spectrum of the signal photons is shown in Fig. S4. Orange triangles show the spectrum in the central region of the interference pattern which correspond to the orange dashed circle in Fig. S2A,B. The black dots show the spectrum integrated across the whole detection region, shown by the black dashed circle in Fig. S2A,B. Figure S4 illustrates that the central wavelength of the SPDC λ_0 varies depending on the scattering angles. The full width at the half maximum of the central spot is 1.91±0.02 nm with the corresponding linewidth of the correlated IR photon calculated to be 42.8±0.4 nm.

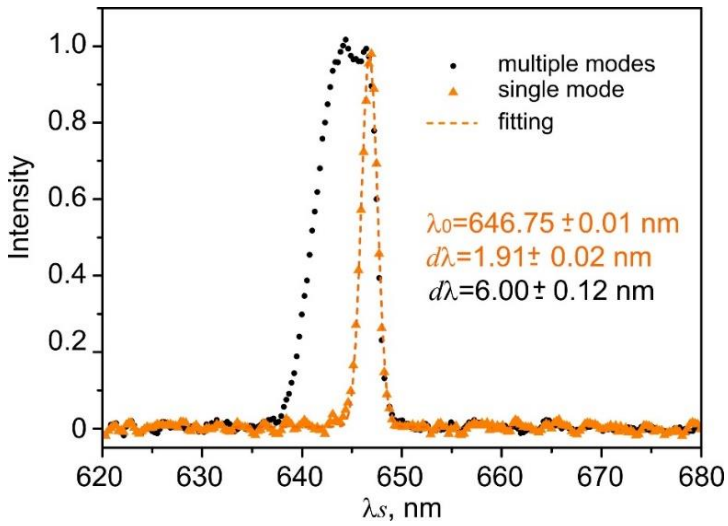

Fig. S4. The normalized spectrum of the signal photons obtained in different areas of the detected interference pattern. Orange triangles show the spectrum obtained at the center of the image, and black dots show the spectrum obtained across the full field of view. Both regions are shown in Fig. S2A,B by orange and black circles, respectively.

5. Further setup optimization

Spatial resolution

Taking into account Eq. (S3), the spatial resolution of the method can be improved by modifying the ratio of focal lengths $f_1 f_3/f_2$. To demonstrate this, we recently performed additional measurements using f_3=2 mm lens (see Fig. S5), which theoretically gives 7.5 μm diffraction limit, according to Eq. (S3). The experiment was done using a 20 mm long PPLN crystal. In this configuration, we achieved ~10 μm resolution (region 5-5 in the USAF1951 resolution test), which is close to the theoretical limit.

The spatial resolution in our method also determined by the aperture of the nonlinear crystal. Therefore, the resolution of the method can be further improved by using a crystal with a larger aperture. For example, using a crystal with an aperture of 5×5 mm^2 and a lens system with f_3=2 mm, it is possible to achieve the resolution down to 2 μm, which is close to the diffraction limit of imaging at 3 μm wavelength.

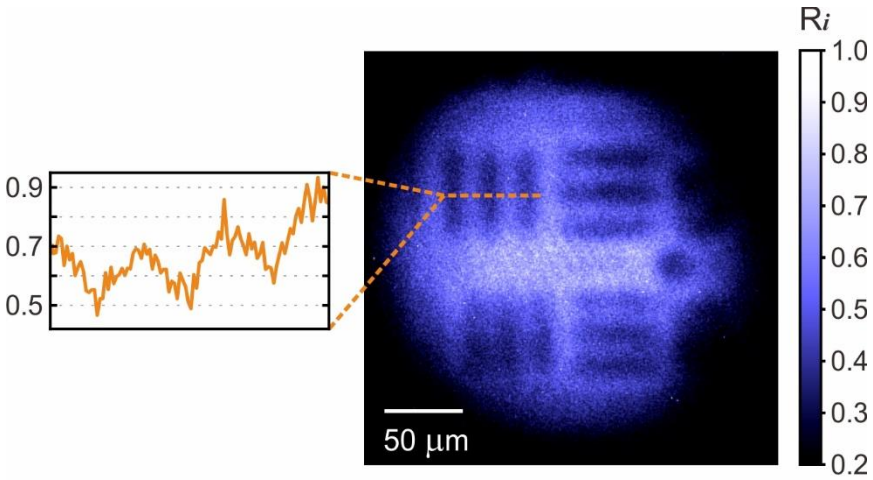

Fig. S5. Reflectivity of the resolutions test target. Imaging wavelength is 3 μm, and the lens focal length is f_3=2 mm. Every step of the piezo stage is recorded for 250 ms. Inset shows the horizontal cross-section of the image.

Spectral resolution

The width of the SPDC spectrum is inversely proportional to the length of the nonlinear element. Hence, the spectral resolution of the method can be further improved by using longer crystals. In our experiment, we used a 10 mm long PPLN crystal, with the spectral

width of the probing signal, and IR beams equal to 1.9 nm and 43 nm, respectively. We made additional measurements for a 20 mm long PPLN crystal, see Fig. S6. The spectrum of the signal and idler photons became narrower and equal to 1.2 nm and 26 nm, respectively.

Thus, by using a 40 mm PPLN crystal, it is possible to achieve spectral bandwidth of ~10 nm (~11 cm^{-1}) at around 3 μm probe wavelength. Though ~11 cm^{-1} is still larger than the value for state of the art conventional techniques (~2 cm^{-1}), it is good enough to probe relatively broad absorption lines at mid-IR range, e.g. –OH stretching (4000 - 3000 cm^{-1}) or –CH stretching (3100 - 2800 cm^{-1}). We also note that using longer nonlinear crystals would not only increase the spectral resolution of the method but also enhance the rate of generated photons and hence reduce the measurement time.

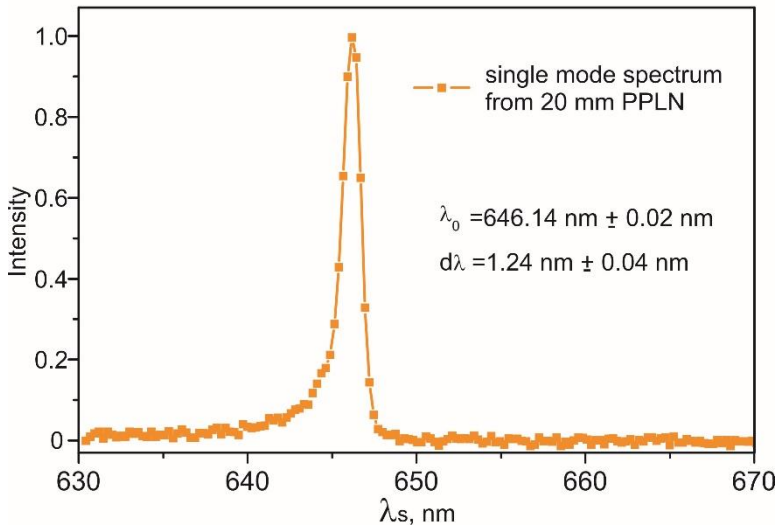

Fig. S6. The normalized spectrum of the signal photons. The 20 mm PPLN crystal is pumped by the 532 nm wavelength laser. The central wavelength of signal photons is 646 nm, which corresponds to the wavelengths of 3015 nm for idler photons.

Measurement time

In the current setup, it takes about ~25 minutes (70s × 21 images) to retrieve the hyperspectral image in the spectral range from 2.8 to 3.4 μm (step of ~25 nm). For the spectral range from 2.5 to 5 μm, the measurement would take about ~100 minutes.

By further optimization of the method, it is possible to reduce the imaging time by technical means, such as by changing to a more sensitive CMOS camera, using longer nonlinear crystal and higher power laser.

In additional experiments with a 20 mm PPLN crystal, presented in Fig. S6, we reduced the detection time by a factor of 2 yet preserving the image quality. We also note that it is possible to decrease the measurement time by using a more powerful pump laser (cw or pulsed). Indeed, cw lasers with ~W power and pulsed lasers with ~mJ energy are readily available in the visible range. A significant advantage of our scheme is that the sample does not interact with the pump beam (unlike in Raman and fluorescence microscopy), which eliminates the risk of damaging and photo-bleaching the sample.

6. <u>Raw visibility data</u>

At the experiment, we obtain the visibility of the interference pattern first. The raw visibility data at the three probing wavelengths are shown in Fig. S7. Then, based on the visibility data we retrieve the absorption map of the sample.

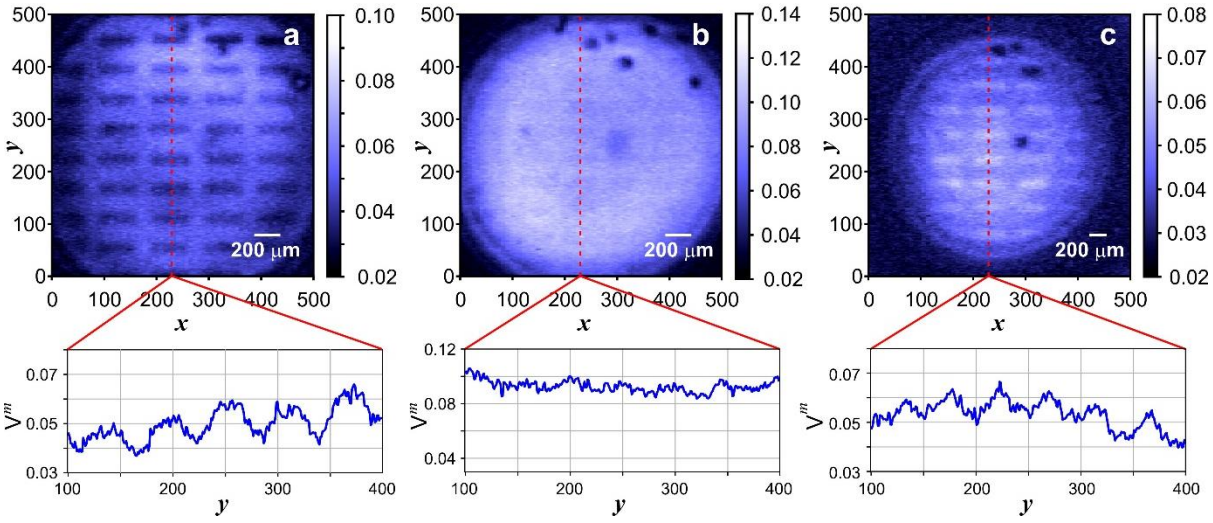

Fig. S7. Raw data of the visibility maps. Visibility map of the interference at (**A**) 2.87 μm, (**B**) 3.18 μm and (**C**) 3.32 μm probe wavelengths. The red dashed lines correspond to the cross-sections shown at the bottom of each picture. The horizontal axis in inserts are number of pixels of the CMOS camera.

REFERENCES AND NOTES

1. R. Bhargava, Infrared spectroscopic imaging: The next generation. *Appl. Spectrosc.* **66**, 1091–1120 (2012).
2. J. E. Katon, Infrared microspectroscopy: A review of fundamentals and applications. *Micron* **27**, 303–314 (1996).
3. P. Colarusso, L. H. Kidder, I. W. Levin, J. C. Fraser, J. F. Arens, E. N. Lewis, Infrared spectroscopic imaging: From planetary to cellular systems. *Appl. Spectrosc.* **52**, 106A–120A (1998).
4. M. J. Baker, J. Trevisan, P. Bassan, R. Bhargava, H. J. Butler, K. M. Dorling, P. R. Fielden, S. W. Fogarty, N. J. Fullwood, K. A. Heys, C. Hughes, P. Lasch, P. L. Martin-Hirsch, B. Obinaju, G. D. Sockalingum, J. Sulé-Suso, R. J. Strong, M. J. Walsh, B. R. Wood, P. Gardner, F. L. Martin, Using Fourier transform IR spectroscopy to analyze biological materials. *Nat. Protoc.* **9**, 1771–1791 (2014).
5. D. A. Moss, M. Keese, R. Pepperkok, IR microspectroscopy of live cells. *Vib. Spectrosc.* **38**, 185–191 (2005).
6. M. Diem, M. Romeo, C. Matthäus, M. Miljkovic, L. Miller, P. Lasch, Comparison of Fourier transform infrared (FTIR) spectra of individual cells acquired using synchrotron and conventional sources. *Infrared Phys. Technol.* **45**, 331–338 (2004).
7. M. R. Kole, R. K. Reddy, M. V. Schulmerich, M. K. Gelber, R. Bhargava, Discrete frequency infrared microspectroscopy and imaging with a tunable quantum cascade laser. *Anal. Chem.* **84**, 10366–10372 (2012).
8. S. Mittal, K. Yeh, L. S. Leslie, S. Kenkel, A. Kajdacsy-Balla, R. Bhargava, Simultaneous cancer and tumor microenvironment subtyping using confocal infrared microscopy for all-digital molecular histopathology. *PNAS* **115**, E5651–E5660 (2018).
9. W. Lei, J. Antoszewski, L. Faraone, Progress, challenges, and opportunities for HgCdTe infrared materials and detectors. *Appl. Phys. Rev.* **2,** 041303 (2015).
10. S. W. Hell, J. Wichmann, Breaking the diffraction resolution limit by stimulated emission: Stimulated-emission-depletion fluorescence microscopy. *Opt. Lett.* **19**, 780–782 (1994).
11. T. D. Lacoste, X. Michalet, F. Pinaud, D. S. Chemla, A. P. Alivisatos, S. Weiss, Ultrahigh-resolution multicolor colocalization of single fluorescent probes. *PNAS* **97**, 9461–9466 (2000).

12. L. Schermelleh, P. M. Carlton, S. Haase, L. Shao, L. Winoto, P. Kner, B. Burke, M. C. Cardoso, D. A. Agard, M. G. Gustafsson, H. Leonhardt, J. W. Sedat, Subdiffraction multicolor imaging of the nuclear periphery with 3D structured illumination microscopy. *Science* **320**, 1332–1336 (2008).
13. M. F. Juette, T. J. Gould, M. D. Lessard, M. J. Mlodzianoski, B. S. Nagpure, B. T. Bennett, S. T. Hess, J. Bewersdorf, Three-dimensional sub-100 nm resolution fluorescence microscopy of thick samples. *Nat. Methods* **5**, 527–529 (2008).
14. A. Dazzi, C. B. Prater, AFM-IR: Technology and applications in nanoscale infrared spectroscopy and chemical imaging. *Chem. Rev.* **117**, 5146–5173 (2017).
15. M. Schnell, S. Mittal, K. Falahkheirkhah, A. Mittal, K. Yeh, S. Kenkel, A. Kajdacsy-Balla, P. S. Carney, R. Bhargava, All-digital histopathology by infrared-optical hybrid microscopy. *PNAS* **117**, 3388–3396 (2020).
16. E. O. Potma, S. Mukamel, Theory of coherent raman scattering, in *Coherent Raman Scattering Microscopy*, J.-X. Cheng, X. S. Xie, Eds. (CRC Press, 2018).
17. S. Junaid, S. Chaitanya Kumar, M. Mathez, M. Hermes, N. Stone, N. Shepherd, M. Ebrahim-Zadeh, P. Tidemand-Lichtenberg, C. Pedersen, Video-rate, mid-infrared hyperspectral upconversion imaging. *Optica* **6**, 702–708 (2019).
18. X. Y. Zou, L. J. Wang, L. Mandel, Induced coherence and indistinguishability in optical interference. *Phys. Rev. Lett.* **67**, 318–321 (1991).
19. L. J. Wang, X. Y. Zou, L. Mandel, Induced coherence without induced emission. *Phys. Rev. A* **44**, 4614–4622 (1991).
20. C. K. Hong, L. Mandel, Theory of parametric frequency down conversion of light. *Phys. Rev. A* **31,** 2409–2418 (1985).
21. D. N. Klyshko, *Photons and Nonlinear Optics* (CRC Press, Boca Raton, FLA, 1988).
22. G. B. Lemos, V. Borish, G. D. Cole, S. Ramelow, R. Lapkiewicz, A. Zeilinger, Quantum imaging with undetected photons. *Nature* **512**, 409–412 (2014).
23. A. V. Paterova, H. Z. Yang, C. W. An, D. A. Kalashnikov, L. A. Krivitsky, Tunable optical coherence tomography in the infrared range using visible photons. *Quantum Sci. Technol.* **3**, 025008 (2018).
24. A. Vallés, G. Jiménez, L. J. Salazar-Serrano, J. P. Torres, Optical sectioning in induced coherence tomography with frequency-entangled photons. *Phys. Rev. A* **97**, 023824 (2018).

25. S. P. Kulik, G. A. Maslennikov, S. P. Merkulova, A. N. Penin, L. K. Radchenko, V. N. Krasheninnikov, Two-photon interference in the presence of absorption. *J. Exp. Theor. Phys.* **98**, 31–38 (2004).
26. D. A. Kalashnikov, A. V. Paterova, S. P. Kulik, L. A. Krivitsky, Infrared spectroscopy with visible light. *Nat. Photonics* **10**, 98–101 (2016).
27. A. V. Paterova, S. Lung, D. A. Kalashnikov, L. A. Krivitsky, Nonlinear infrared spectroscopy free from spectral selection. *Sci. Rep.* **7**, 42608 (2017).
28. A. V. Paterova, H. Z. Yang, C. W. An, D. A. Kalashnikov, L. A. Krivitsky, Measurement of infrared optical constants with visible photons. *New J. Phys.* **20**, 043015 (2018).
29. A. V. Paterova, L. A. Krivitsky, Nonlinear interference in crystal superlattices. *Light Sci. Appl.* **9**, 82 (2020).
30. M. Kutas, B. Haase, P. Bickert, F. Riexinger, D. Molter, G. von Freymann, Terahertz quantum sensing. *Sci. Adv.* **6**, eaaz8065 (2020).
31. S. P. Walborn, C. H. Monken, S. Pádua, P. H. Souto Ribeiro, Spatial correlations in parametric down-conversion. *Phys. Rep.* **495**, 87–139 (2010).
32. T. P. Grayson, G. A. Barbosa, Spatial properties of spontaneous parametric down-conversion and their effect on induced coherence without induced emission. *Phys. Rev. A* **49**, 2948–2961 (1994).
33. E. G. Steward, *Fourier Optics: An Introduction* (Dover Publications, New York, ed. 2, 2004).
34. M. Lahiri, R. Lapkiewicz, G. B. Lemos, A. Zeilinger, Theory of quantum imaging with undetected photons. *Phys. Rev. A* **92**, 013832 (2015).
35. T. J. Herzog, J. G. Rarity, H. Weinfurter, A. Zeilinger, Frustrated two-photon creation via interference. *Phys. Rev. Lett.* **72**, 629–632 (1994).
36. L. E. Myers, G. D. Miller, R. C. Eckardt, M. M. Fejer, R. L. Byer, W. R. Bosenberg, Quasi-phase-matched 1064-μm-pumped optical parametric oscillator in bulk periodically poled LiNbO3. *Opt. Lett.* **20**, 52–54 (1995).
37. L. E. Myers, R. C. Eckardt, M. M. Fejer, R. L. Byer, W. R. Bosenberg, Multigrating quasi-phase-matched optical parametric oscillator in periodically poled LiNbO3. *Opt. Lett.* **21**, 591–593 (1996).

38. E. Mitri, G. Birarda, L. Vaccari, S. Kenig, M. Tormen, G. Grenci, SU-8 bonding protocol for the fabrication of microfluidic devices dedicated to FTIR microspectroscopy of live cells. *Lab Chip* **14**, 210–218 (2014).
39. C. Moissl-Eichinger, A. J. Probst, G. Birarda, A. Auerbach, K. Koskinen, P. Wolf, H-Y. N. Holman, Human age and skin physiology shape diversity and abundance of Archaea on skin. *Sci. Rep.* **7**, 4039 (2017).
40. M. V. Chekhova, Z. Y. Ou, Nonlinear interferometers in quantum optics. *Adv. Opt. Photonics* **8**, 104–155 (2016).
41. A. V. Burlakov, M. V. Chekhova, D. N. Klyshko, S. P. Kulik, A. N. Penin, Y. H. Shih, D. V. Strekalov, Interference effects in spontaneous two-photon parametric scattering from two macroscopic regions. *Phys. Rev. A* **56**, 3214–3225 (1997).
42. A. V. Paterova, H. Yang, Ch. An, D. A. Kalashnikov, L. A. Krivitsky, Polarization effects in nonlinear interference of down-converted photons. *Opt. Express* **27**, 2589–2603 (2019).
43. G. Frascella, E. E. Mikhailov, N. Takanashi, R. V. Zakharov, O. V. Tikhonova, M. V. Chekhova, Wide-field SU(1,1) interferometer. *Optica* **6**, 1233–1236 (2019).
44. A. Heuer, R. Menzel, P. W. Milonni, Complementarity in biphoton generation with stimulated or induced coherence. *Phys. Rev. A* **92**, 033834 (2015).
45. A. C. Cardoso, L. P. Berruezo, D. F. Ávila, G. B. Lemos, W. M. Pimenta, C. H. Monken, P. L. Saldanha, S. Pádua, Classical imaging with undetected light. *Phys. Rev. A* **97**, 033827 (2018).
46. M. Born, E. Wolf, *Principles of Optics* (Cambridge Univ. Press, Cambridge, 1999).
47. S. Ashraf, I. Niskanen, B. Kanyathare, E. Vartiainen, C. Mattsson, R. Heikkilä, G. Thungström, Determination of complex refractive index of SU-8 by Kramers–Kronig dispersion relation method at the wavelength range 2.5–22.0 μm. *J. Quant. Spectrosc. Radiat. Transfer* **224**, 309–311 (2019).
48. D. F. Edwards, E. Ochoa, Infrared refractive index of silicon. *Appl. Optics* **19**, 4130–4131 (1980).
49. H. H. Li, Refractive index of alkaline earth halides and its wavelength and temperature derivatives. *J. Phys. Chem. Ref. Data Monogr.* **9**, 161–290 (1980).
50. A. Ling, A. Lamas-Linares, C. Kurtsiefer, Absolute emission rates of spontaneous parametric down-conversion into single transverse Gaussian modes. *Phys. Rev. A* **77**, 043834 (2008).